



Article

Examining the Impact of Intermediate Cooling on Mechanical Properties of 22MnB5 in a Tailored Tempering Process [†]

Alborz Reihani ^{1,*}, Sebastian Heibel ¹, Thomas Schweiker ¹ and Marion Merklein ²

¹ Mercedes-Benz AG, Béla-Barényi-Straße 1, 71059 Sindelfingen, Germany;

sebastian.heibel@mercedes-benz.com (S.H.); thomas.schweiker@mercedes-benz.com (T.S.)

² Institute of Manufacturing Technology (LFT), Friedrich-Alexander-Universität Erlangen-Nürnberg, Egerlandstraße 13, 91058 Erlangen, Germany; marion.merklein@fau.de

* Correspondence: alborz.reihani_masouleh@mercedes-benz.com; Tel.: +49-(0)-160-8694430

[†] This paper is an extended version of our paper “Alborz Reihani, Sebastian Heibel, Thomas Schweiker, Marion Merklein. Examination of controlled thermal radiation exchange for the production of tailored properties on press-hardened components”. In Proceedings of the 20th International Conference on Sheet Metal (SHEMET 2023), Erlangen-Nürnberg, Germany, 2–5 April 2023.

Abstract: Tailoring the properties of hot-stamped components offers the potential to enhance crash performance while simultaneously improving downstream joining processes. In recent years, an innovative technology suited for achieving tailored properties involving the utilization of a specialized furnace chamber, known as the TemperBox[®], has been introduced. Within this chamber, a cooled aluminum mask shields specific areas of the blank from incoming heat radiation and concurrently absorbs the blank’s own radiation. The duration of the heat radiation exchange can influence the diffusion-dependent phase transformation and, consequently, the resulting mechanical properties. Hence, the intermediate cooling duration assumes a pivotal role as a parameter, as is investigated in this study. To examine the effects, specimens of the steel 22MnB5 AS150 are subjected to intermediate cooling of varying durations, followed by forming and partial quenching. The temperature profile of the blank during intermediate cooling prior to forming and quenching is analyzed. Subsequently, the tailored hot-stamped components are assessed for hardness, strength, ductility, and thickness strain. The study reveals that with increasing duration of partial intermediate cooling and targeted radiation exchange, a homogeneous ferritic–pearlitic structure is formed from an austenitic structure. This uniform structure of ferrite and pearlite is reflected in lower hardness and strength values, along with improved ductility. Additionally, this paper introduces a simulation methodology designed to calculate the dynamics of thermal radiation and the kinetics of phase transformation.

Keywords: tailored tempering; hot stamping; heat exchange; simulation; heat radiation dynamics; view factor



Citation: Reihani, A.; Heibel, S.; Schweiker, T.; Merklein, M. Examining the Impact of Intermediate Cooling on Mechanical Properties of 22MnB5 in a Tailored Tempering Process. *J. Manuf. Mater. Process.* **2024**, *8*, 5. <https://doi.org/10.3390/jmmp8010005>

Received: 29 November 2023

Revised: 22 December 2023

Accepted: 24 December 2023

Published: 26 December 2023



Copyright: © 2023 by the authors. Licensee MDPI, Basel, Switzerland. This article is an open access article distributed under the terms and conditions of the Creative Commons Attribution (CC BY) license (<https://creativecommons.org/licenses/by/4.0/>).

1. Introduction

Statutory mandates aimed at diminishing greenhouse gas emissions are compelling the automotive industry to innovative concepts, such as electric or hydrogen-based propulsion systems [1]. Considering the higher overall weight of these propulsion systems in comparison to internal combustion engines, lightweight construction, and lightweight materials emerge as key technologies for ensuring compliance with these regulations. Simultaneously, the challenge lies in meeting the increased crash safety requirements in modern vehicles [2]. In addition to materials like high-strength cold-formable steels and aluminum, there is a growing utilization of body components made from hot-stamped steels [3]. Through a combination of forming in the austenitized state and subsequent quenching, conventional hot-stamped steels like 22MnB5 can achieve tensile strengths of about 1500 MPa [4]. The high tensile strength enables the use of thin-walled, weight-optimized components in highly stressed structural areas of the body. However, research

findings consistently indicate that the crash performance of structural components, as well as the mechanical joinability and cutability in rework processes, can be optimized through the deliberate incorporation of regions with reduced strength and enhanced ductility [5]. The increasing demands in terms of component complexity and properties cannot be met with conventionally manufactured 22MnB5 hot-stamped components. The utilization of new semi-finished products and functionally adapted component concepts, including tailor rolled blanks, tailor welded blanks, patchwork blanks, and tailor tempered parts, offers the opportunity to integrate ductile component areas and expand the boundaries for the application of structural components [6]. The concept of tailor tempered parts has assumed an important role, primarily attributed to continuous advancements in tool and furnace technology. To produce tailor tempered parts, four distinct process control strategies can be identified concerning partial austenitization and partial intermediate cooling prior to quenching, partial cooling during the quenching phase, and partial tempering post-quenching [6].

One approach of tailored tempering with intermediate cooling is facilitated by a furnace chamber known as the TemperBox[®], which was developed by Gedia GmbH Attendorn, Germany. This specialized furnace chamber is integrated into a multi-chamber furnace manufactured by AP&T AB and enables the production of hot-stamped components with graded mechanical properties through partial intermediate cooling. A crucial component of the TemperBox[®] comprises two water-cooled aluminum masks, between which the heated blank is positioned and locally cooled in covered areas. The process steps of tailored hot stamping with the TemperBox[®] are shown in Figure 1a.

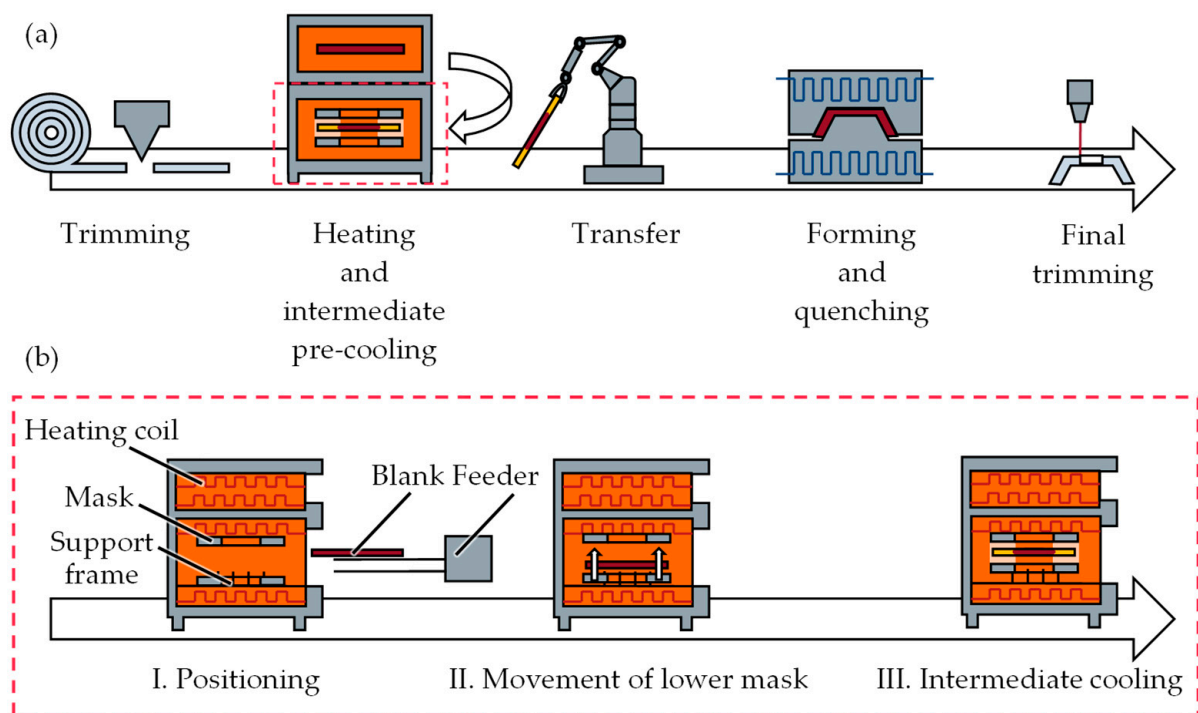


Figure 1. (a) Process steps of tailored hot stamping with TemperBox[®] (b) and process steps within TemperBox[®].

Initially, the raw material is trimmed and heated. The heating duration required to achieve uniform austenitization varies according to the blank geometry, material type, and sheet thickness. Subsequently, the austenitized blank is automatically positioned within the TemperBox[®] and subjected to an intermediate cooling phase. The processes within the TemperBox[®] (Figure 1b) can be segmented into three distinct stages: I. positioning; II. movement of the lower mask; and III. intermediate cooling. In the first stage, the uniformly austenitized blank is positioned on the support frame within 4 to 6 s. The lower

movable mask then moves towards the upper fixed mask, securely centering the blank with the aid of centering cones. Depending on the blank's geometry, material properties, and sheet thickness, the intermediate cooling process takes approximately 45 to 140 s, employing a cooled aluminum mask. The surface of the mask facing the heating elements is chrome-plated and polished to a mirror-like finish to minimize heat absorption. In contrast, the mask side facing the blank is intentionally given a higher surface roughness to enhance the absorption of thermal radiation emitted by the heated blank. After the intermediate cooling stage, the blank is positioned in the tool, accomplished using a robotic system or furnace feeder. Within the tool, the blank undergoes both forming and partial quenching. During the quenching phase, the blank's cooling process begins due to the thermal energy transfer upon contact with the tool. The heat conduction effect results in the non-diffusion transformation of the austenitized region of the blank into a martensitic microstructure due to rapid cooling. The effect of heat conduction on the phase transformation within the covered area of the blank depends on the duration of intermediate cooling and the preceding phase transformation from austenite to ferrite, pearlite, and bainite. Once quenched, the components are air-cooled and subsequently trimmed to their final dimensions. A significant advantage of the process route involving intermediate cooling, in comparison to alternative tailored tempering methods using heated tools or localized laser annealing, is the improved dimensional accuracy of the components [7]. This improvement is a result of the reduced temperature gradient experienced by the components after quenching in the cooled tools. Moreover, this process allows for the adjustment of soft, transition, and hard areas by modifying process parameters, such as the distance between the blank and the aluminum mask or the duration of intermediate cooling within the TemperBox[®]. Additionally, the approach leads to consistent surface properties, in contrast to methods that involve partial austenitization. With partial austenitization approaches, the coating varies due to different heating rates [8]. Precisely controlling the heat treatment within these process pathways enhances the ductility in areas of the components with lower strength. This increased ductility results in enhanced energy absorption and deformation capacity during crash-like events, as well as simplifying subsequent mechanical joining operations.

The impact of intermediate cooling through radiation exchange within a tailored hot stamping process on phase transformation and component properties has not been experimentally investigated in scientific studies. For this reason, this study examines the impact of the duration of partial intermediate cooling by radiation exchange in a partial press hardening process on the diffusion-dependent phase transformation process and the component properties using the conventional manganese-boron steel 22MnB5. The experiments are conducted using a chamber furnace provided by AP&T AB, equipped with two chambers for heating and austenitization of the blank, along with the TemperBox[®] for partial intermediate cooling of the blank. In this context, partial intermediate cooling of the blank is defined as cooling the covered areas while continuing to heat the uncovered areas, which remain in the austenitic state. In addition to the controlled exchange of heat radiation, the time- and temperature-dependent phase transformations are important and play a key role in achieving tailored properties in hot-stamped components. To explore these effects, this study presents an approach to simulate radiative heat exchange in the LS-Dyna[®](R12) program. The simulation results are validated through experimental investigations.

2. Fundamentals of Phase Transformation and Radiant Heat Exchange in Hot Stamping

In recent decades, finite element analysis has emerged as the established simulation method in the field of engineering [9]. The main objectives are to expedite the design and development phases and to facilitate manufacturability assessment. In the field of hot stamping, accurate prediction of phase transformation processes and their subsequent impact on component properties assumes critical importance for optimizing the manufacturing process. To model the intricate thermomechanical interactions that take place during hot stamping and to account for the influence of phase transformation behavior, a profound

understanding of various mechanical, thermal, and microstructural influencing factors is imperative [10]. In particular, the determination of the austenite decomposition into ferrite, pearlite, bainite, and martensite is important when simulating hot stamping processes.

The transformation kinetics for these phases are mainly diffusion-controlled, except for martensite transformation, and can be described by various models. [11]. A well-established model that adopts a phenomenological approach was formulated by Johnsen, Mehl, Avrami, and Kolmogorov (JMAK) and is commonly referred to as the incremental variant of the JMAK model [12]. This incremental form of the JMAK model addresses the phase transformation that occurs during isothermal processes. To calculate non-isothermal processes, like hot stamping and welding, the JMAK model has been extended through various approaches [13]. In addition to the JMAK model, Kirkaldy-type semi-empirical transformation models are also utilized for the computation of the phase transformation process [14]. As an example, Li et al. [15] formulated a model based on the framework of Kirkaldy and Venugopalan [16] in which the phase transformation is contingent upon various factors, including grain number, chemical composition, temperature, and activation energy of distinct phases. It differs from the Kirkaldy model in terms of the influence of the chemical composition and the grain number. The transformation of austenite into martensite takes place abruptly and is not governed by a diffusion process. To represent this phase transformation, the non-diffusion phase transformation Koistinen–Marburger model [17] is employed.

The following section offers an overview of the fundamental principles involved in calculating heat radiation exchange and delves into application-specific aspects of partial intermediate cooling using the TemperBox[®]. Depending on the stage of the process, various heat transfer mechanisms become relevant in hot stamping. In the transfer phase, the temperature of the blank decreases due to heat radiation and convection with the surrounding environment. Additionally, during the forming and quenching phases, there is an added heat conduction element resulting from the contact with the tool. Advancements in technology, both in the equipment and tooling domains, have introduced greater intricacies to the thermal challenge. For instance, in the case of the TemperBox[®], the interaction of heat radiation between surfaces within an enclosure assumes a distinct significance. Unlike heat transfer mechanisms like convection and heat conduction, where heat energy is transported from warmer to cooler areas, heat radiation involves the exchange of heat energy from cooler to warmer areas [18]. The effectiveness of this heat radiation exchange is particularly influenced by factors such as the orientation and position of the emitting surfaces, their respective temperatures, and their radiation properties [18].

A geometric parameter employed to streamline the computation of heat radiation exchange is known as the view factor. The view factor quantifies the proportion of heat radiation transferred from one surface to another, contingent on their respective positions and orientations, without regard to the wavelength of the thermal radiation [18]. The derivation of the view factor begins with the photometric fundamental law. For two surfaces located in an empty space, as depicted in Figure 2a, the photometric fundamental law provides the radiant flow, denoted as $d^2\varphi_{ij}$, from a small surface increment (dA_i) to another small surface increment (dA_j). This radiant flow is expressed as a function of the surface's intensity (L_i) and the distance (S) between the surfaces and the angles (θ_i), as well as (θ_j) between the common connecting line and the normal vector of the surfaces [18]:

$$d^2\varphi_{ij} = L_i \frac{\cos\theta_i \cos\theta_j}{S^2} dA_i dA_j. \quad (1)$$

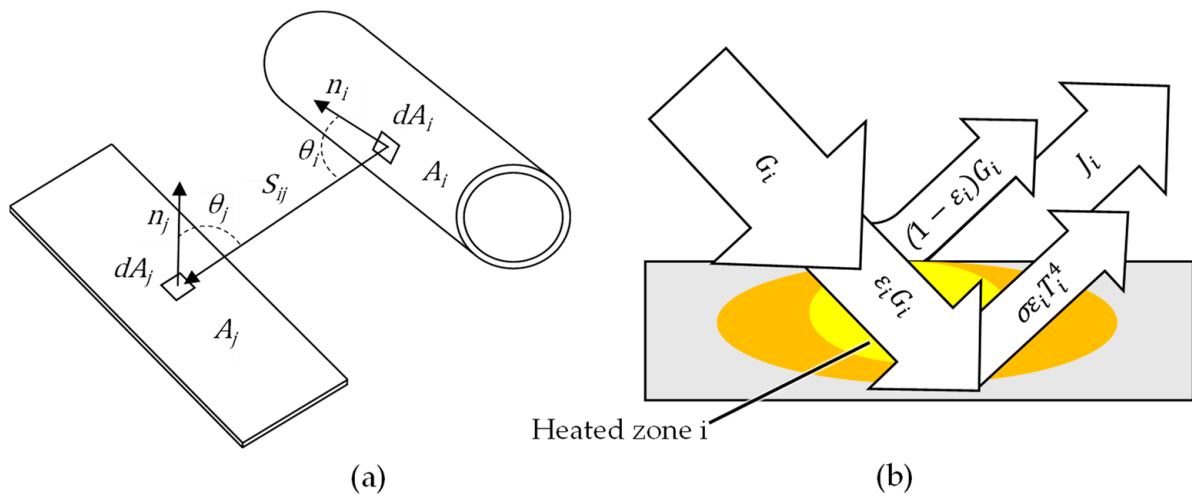


Figure 2. (a) Two finite surfaces and their orientation and position in an empty space; (b) The representation of radiation energy exchange on zone i according to [18].

Through the integration of the photometric fundamental law, as defined in Equation (1), across two finite surfaces and under the assumption of a constant radiation intensity (L_i) over the surface, the radiation flow can be described by the following equation:

$$\varphi_{ij} = L_i \int_{A_i} \int_{A_j} \frac{\cos\theta_i \cos\theta_j}{S^2} dA_i dA_j. \tag{2}$$

With the relation $\varphi_i = \pi L_i A_i$ as the radiant flux emitted from the surface (A_i), the view factor is obtained as:

$$F_{ij} := \frac{\varphi_{ij}}{\varphi_i} = \delta_{ij} \frac{1}{A_i} \int_{A_i} \int_{A_j} \frac{\cos\theta_i \cos\theta_j}{\pi S^2} dA_i dA_j. \tag{3}$$

Equation (3) reveals that the view factor is a geometric parameter that quantifies the proportion of radiation emitted from surface (A_i) to surface (A_j). In this context, the Kronecker delta (δ_{ij}) characterizes the visibility between finite surfaces. Surfaces that have line-of-sight visibility to each other are assigned a value of 1, while surfaces lacking such visibility are assigned a value of 0.

Radiation exchange problems in the LS-Dyna[®] simulation program are solved using the energy balance at zone i, as depicted in Figure 2b. The heat flow (\dot{Q}_i) can be expressed as the difference between emitted radiation (J_i) and irradiation (G_i) [18]. As emitted radiation already accounts for the reflected radiation of irradiation (G_i), the equation for heat flow (\dot{Q}_i) can be simplified as follows:

$$\dot{Q}_i = A_i (J_i - G_i) = \frac{A_i \epsilon_i}{(1 - \epsilon_i)} (\sigma T_i^4 - J_i) \tag{4}$$

where ϵ_i represents the emissivity, σ denotes the Stefan–Boltzmann constant, and T_i signifies the temperature of zone i. By connecting the incident radiant flux $A_i G_i$ with all the other zones, a secondary relationship between the heat flow (\dot{Q}_i) and emitted radiation (J_i) is derived. In conjunction with the reciprocity law $A_j F_{ji} = A_i F_{ij}$, the total radiation incident on zone i can be described as follows [19]:

$$A_i G_i = \sum_{j=1}^n A_j F_{ji} J_j = A_i \sum_{j=1}^n F_{ij} J_j \tag{5}$$

By substituting Equation (5) into Equation (4), the heat flow (\dot{Q}_i) can be described by the following equation:

$$\dot{Q}_i = A_i(J_i - \sum_{j=1}^n F_{ij}J_j) = A_i\sum_{j=1}^n F_{ij}(J_i - J_j) \tag{6}$$

Equating Equations (4) and (6), the unknown heat flow (\dot{Q}_i) can be eliminated and the radiation problem can be solved by the following equation:

$$A_i(J_i - (1 - \epsilon_i)\sum_{j=1}^n F_{ij}J_j) = A_i\epsilon_i\sigma T_i^4, \quad i = 1, 2, \dots, m \tag{7}$$

Equation (7) is used for zones 1, 2 ... m, where the temperature (T_i) of the zone i is given and all coefficients are known. In matrix form, Equation (7) is called the radiosity model or radiosity matrix equation and can be formulated as follows [19]:

$$\begin{bmatrix} A_1 - (1 - \epsilon_1)A_1F_{11} & -(1 - \epsilon_1)A_1F_{12} & \dots & -(1 - \epsilon_1)A_1F_{1n} \\ -(1 - \epsilon_2)A_2F_{21} & A_2 - (1 - \epsilon_2)A_2F_{22} & \dots & -(1 - \epsilon_2)A_2F_{2n} \\ \vdots & \vdots & \ddots & \vdots \\ -(1 - \epsilon_m)A_mF_{m1} & -(1 - \epsilon_m)A_mF_{m2} & \dots & A_m - (1 - \epsilon_m)A_mF_{mn} \end{bmatrix} \cdot \begin{bmatrix} J_1 \\ J_2 \\ \vdots \\ J_m \end{bmatrix} = \begin{bmatrix} \epsilon_1A_1\sigma T_1^4 \\ \epsilon_2A_2\sigma T_2^4 \\ \vdots \\ \epsilon_mA_m\sigma T_m^4 \end{bmatrix} \tag{8}$$

3. Materials and Methods

3.1. Investigated Material and Experimental Setup

In addition to the conventional hot-stamping parameters, such as transfer time, furnace temperature, holding time in the furnace and the tool, as well as press force, the incorporation of the TemperBox[®] introduces parameters that can significantly influence thermomechanical interactions and the phase transformation during partial intermediate cooling through thermal radiation. These factors include intermediate cooling duration, mask distance to the blank, and mask and blank geometry, as well as the surface properties and temperature of the blank and mask. Since the duration of heat radiation has not been investigated in the scientific context of tailored hot stamping, the influence of intermediate cooling duration on component properties after quenching is a central focus of this study. Within the scope of this research, a test geometry in the form of a hat profile is subjected to tailored hot stamping with intermediate cooling at a test facility of Mercedes-Benz AG. This component is then tested for temperature, hardness, tensile strength, elongation at break, and thickness strain. The corresponding tool halves (Figure 3a) and the dimensions of the blank (Figure 3b) and the component (Figure 3c) are shown in Figure 3.

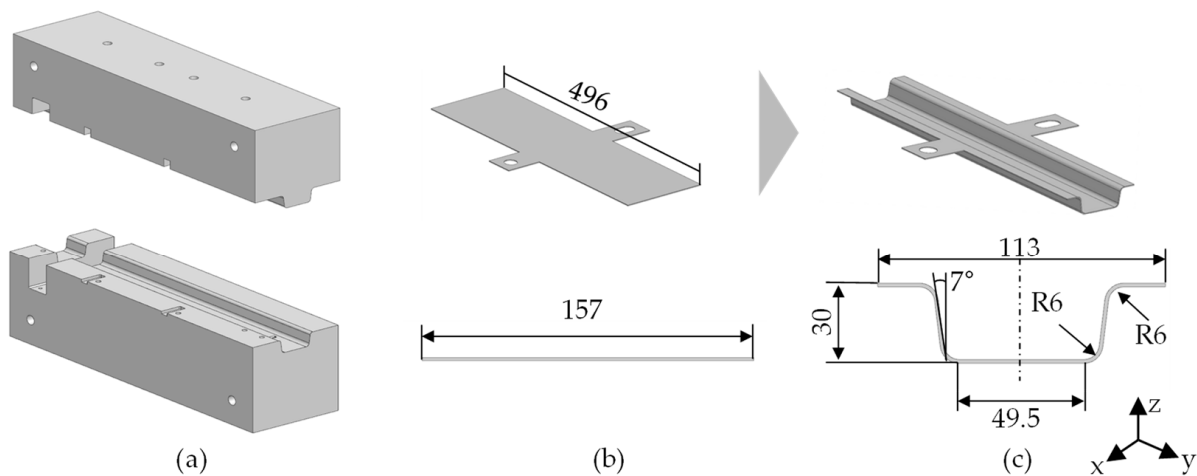


Figure 3. (a) Tool halves as well as dimensions of (b) the blank and (c) the formed test component.

The process steps and key parameters involved in each step of this investigation, from heating to partial quenching of the blank, are outlined below. The outlined temperature profiles in the covered and uncovered regions of the blank, along with the dwell times in the respective process phases, are depicted in Figure 4. The blanks are initially heated in the chamber furnace with a furnace temperature of 950 °C and a furnace holding time of 350 s. Following the heating process, the blanks are transferred by a furnace feeder in 4.5 s from the furnace chamber to the TemperBox[®], where they are positioned on the support frame between the masks.

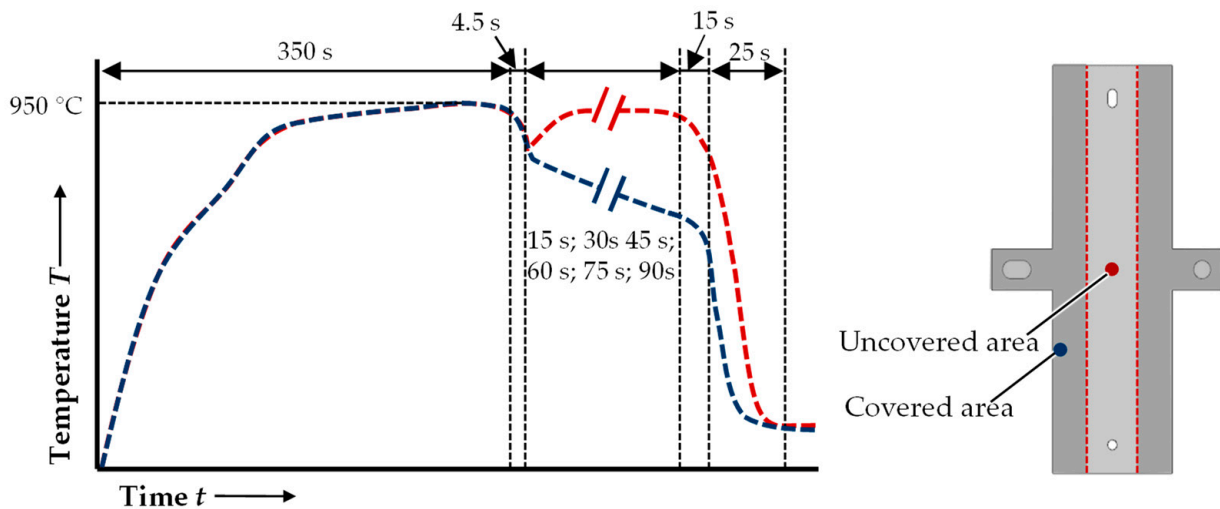


Figure 4. Temperature profile of the blank to investigate the impact of intermediate cooling duration.

Upon positioning, the lower mask is elevated, and the blank is secured by centering cones. To maintain a 2 mm distance between the blank and the mask, as well as to prevent direct contact between them, the blank is supported by pins. Once the blank reaches a distance of 2.0 mm to the upper mask, intermediate cooling commences due to the thermal radiation exchange between the mask and the covered area of the blank (Figure 5a). The duration of the thermal radiation exchange can affect the phase transformation and consequently the mechanical properties in the uncovered and covered areas of the blank. To assess the impact of the duration of heat exchange in the TemperBox[®] on phase transformation, cooling rate, and its importance for the resultant component properties, the blanks undergo partial intermediate cooling with varying durations of 15 s, 30 s, 45 s, 60 s, 75 s, and 90 s. Throughout the partial intermediate cooling phase, the temperature of the blank surface is measured at various intermediate cooling durations using type K thermocouples welded onto the surface of the blank. The measuring points for the covered and uncovered areas of the blank are displayed in Figure 5b. Following the partial intermediate cooling phase, the blanks are subjected to forming and partial quenching in the tool. In this case, the transfer stage until the onset of the forming stage, initiated by the first bilateral tool contact with the blank, lasts for approximately 15 s. During the quenching phase, a holding time of 25 s and a pressing force of 1250kN are applied. To ensure reproducibility, the test cycles are repeated three times for each of the specified intermediate cooling durations.

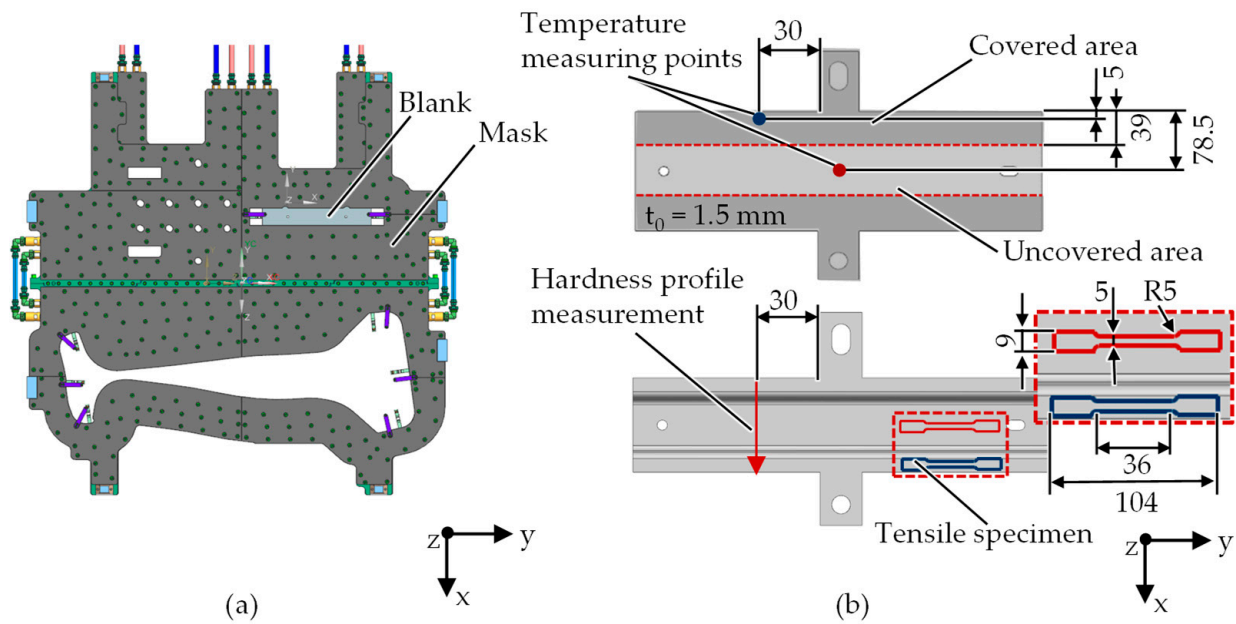


Figure 5. (a) The mask and recess geometry, as well as (b) the tensile specimens and the measuring sections for hardness and temperature measurements.

Following the tailored tempering process, tensile samples are laser-cut from the components (Figure 5b) with a 1 mm allowance on both sides before being milled to their final dimensions. This minimizes the thermal impact of laser cutting and creates a suitable surface with reduced roughness. Tensile tests are conducted using a Z250 RetroLine universal testing machine from Zwick/Roell AG. Prior to measurement, the specimen cross-section (thickness and width) must be measured to allow the software to calculate the applied stress. The data are input into the testXpert III software, which is later employed for visualizing the measurement. Once the specimen is clamped in the hydraulic jaws, the measurement is initiated. During the measurement, the applied tensile force and resulting specimen elongation are recorded using a load cell and a laser extensometer and directly visualized in a stress–strain diagram. The tests are performed in a strain-controlled manner with a clamping pressure of 100 bar, a preload of 5 MPa, a testing speed of 0.0067 mm/s, and a force release of 80%.

To prepare the hardness profile specimens, the specimen is initially cut in half lengthwise and then crosswise using the Struers Discotom-100 tabletop cutting machine, and the cut edges are then deburred. Plastic springs secure the specimens, which are then placed in a 90 mm × 50 mm embedding mold, with two specimens per mold. The cold embedding agent, a mixture of LevoCit powder and LevoCit liquid in a 2:1 ratio from Struers GmbH Willich, Germany is evenly distributed in the embedding mold. The hardened mold undergoes semi-automatic mineralogical preparation in a multi-stage process on the LaboPol-60 grinding and polishing unit, using the LaboForce-100 sample moving unit from Struers GmbH. Grinding is performed with 120-, 220-, and 500-grit grinding pads for 60 s each. The samples are then subjected to a polishing step for 3 min each, using 9 and 3 μm abrasive suspensions. During grinding, the applied contact pressure is 220 N, while during polishing, it is reduced to 180 N. In both processes, the rotational speed of the turntable is set at 300 rpm and that of the sample holder at 150 rpm. Following these procedures, the hardness profile specimens are additionally used to measure the thickness of the components using an optical microscope.

In addition to mechanical characterization of the component properties, the material structure is analyzed. The material structure forms differently depending on the heat treatment and provides important information that can explain the respective material behavior. To analyze the material structure, the prepared samples must be etched after

polishing. For steel materials, nital etching is often used, which consists of three percent nitric acid and alcohol. By etching the samples, the grain boundaries become visible and different phase proportions can be approximately determined. In this study, the samples are analyzed after nital etching using a Leica reflected light microscope and Stream-Enterprise software(2.5).

The material used in these investigations is the micro-alloyed and aluminium–silicon-coated 22MnB5 AS150, initially possessing a sheet thickness (t_0) of 1.5 mm. The chemical composition of 22MnB5 AS150 is provided in Table 1 and the mechanical properties of the as-received material are shown in Table 2.

Table 1. Chemical composition of 22MnB5 in wt. %.

Material/Sheet Thickness	C (%)	Mn (%)	B (%)	Cr (%)	Si (%)	Al (%)	Ti (%)	Ni (%)	Mo (%)
22MnB5/1.50 mm	0.23	1.18	0.003	0.18	0.25	0.03	0.04	0.02	0.003

Table 2. Mechanical properties of as-received 22MnB5.

Material/Sheet Thickness	Tensile Strength T_s (MPa)	Yield Strength Y_s (MPa)	Elongation at Break A (%)
22MnB5/1.50 mm	595	431	21

3.2. Numerical Model

In this study, the simulation program LS-Dyna[®](R12) is used to numerically simulate the tailored tempering process with TemperBox[®]. For the numerical analysis of hot stamping, it is imperative to integrate not only the phase transformation and contact conditions but also the thermomechanical properties. Material models such as “*MAT_244”, “*MAT_248”, and “*MAT_254” facilitate the linkage of thermal properties, temperature and strain rate-dependent hardening behavior, and phase transformation. These models enable the calculation of hot-forming behavior and the final component properties. For modeling the material behavior during heat exchange, the blank is characterized using the material model “*MAT_244”. This material model encompasses thermal-mechanical properties, hardening behavior, and phase transformations, allowing for the prediction of the hot-stamping process and the calculation of hardness in 22MnB5 components [20]. The “*MAT_244” model is based on the results of Åkerstrom and Oldenburg [21]. Within this material model, the phase transformation process, transitioning from austenite to ferrite, pearlite, and bainite, is assumed according to the model developed by Li et al. [15]. The transformation from austenite to martensite is computed using the Koistinen–Marburger model [17]. The initial phase transition temperatures for different phases are obtained from the continuous cooling transformation (CCT) diagram as provided by Aranda et al. [22] and are manually integrated into the material model “*MAT_244” for this study.

In addition to the computational phase transformation, a central component of the numerical model involves the modeling of heat radiation dynamics within the TemperBox[®]. In LS-Dyna[®], a geometric parameter known as the view factor is utilized to determine the fraction of heat radiation that is transmitted from one element to another. Through the computation of view factors in LS-Dyna[®], it is possible to model the exchange of heat radiation between distinct surface segments. Blankenhorn et al. [23] have enhanced and implemented this calculation method in LS-Dyna[®] to represent the radiation exchange within a B-pillar segment inside a paint-curing oven. For the calculation of thermal radiation exchange in this study, the keyword “*BOUNDARY_RADIATION_ENCLOSURE” is employed. Consequently, the TemperBox[®] is depicted as a closed furnace chamber, comprising elements such as the housing, heating elements, masks, and blank. The blank is modeled with solid elements (elform = 3), as shell elements cannot represent the bidirectional radiation exchange due to the unidirectional element normals. The heating

elements, the housing, and the cooled mask in Figure 6 are modeled as shell elements (elform = 16) and thermal isotropic rigid bodies since the initial temperatures and the temperature profile are given as boundary conditions and are not calculated specifically. The essential thermal boundary conditions for calculating radiation exchange and the emissivity coefficients of various materials were consolidated from time-temperature measurements and literature values [24]. The ceramic heating elements are assumed to operate at 1100 °C with an emissivity coefficient of 0.9. Simultaneously, the cooled aluminum mask is regulated within a temperature range of 40 °C to 80 °C. In the simulation's boundary conditions, the aluminum mask is assigned a constant temperature of 50 °C with an emissivity coefficient of 0.2. The housing, incorporating internal insulation materials, is specified at a constant temperature of 100 °C with an emissivity coefficient of 0.8. In addition to the calculation of the radiative heat exchange, the numerical model considers the natural convective heat exchange with the environment.

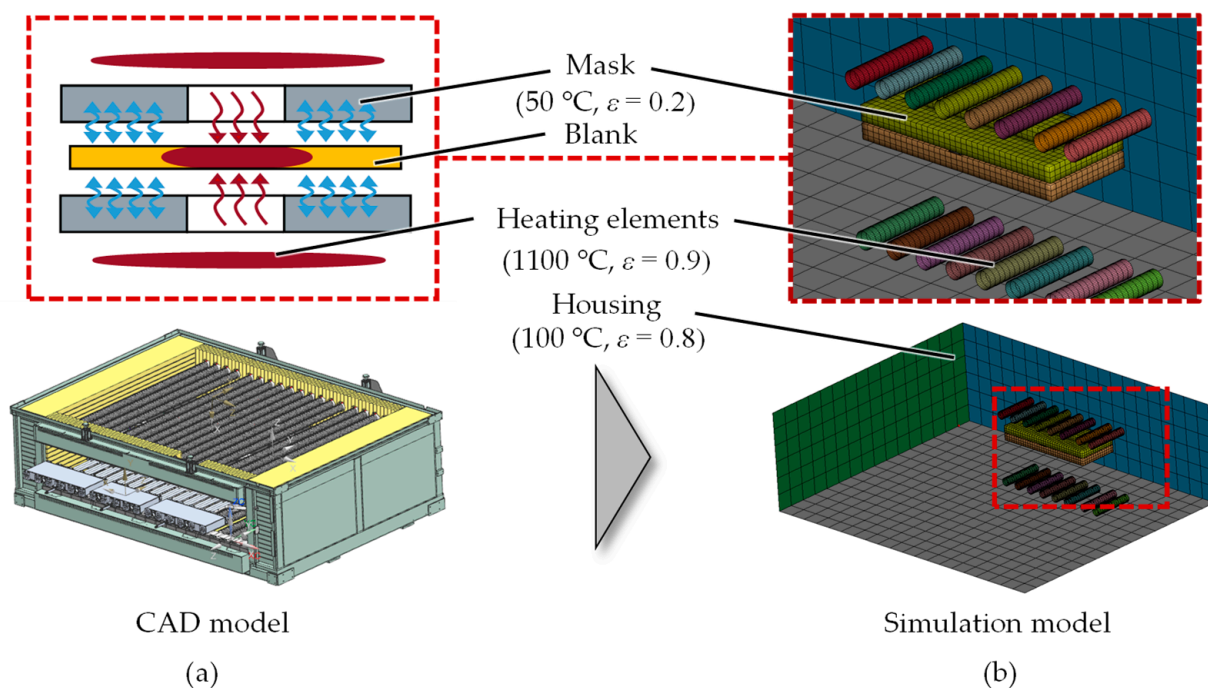


Figure 6. (a) CAD model and corresponding (b) simulation model for the calculation of intermediate cooling by radiation exchange in the TemperBox[®].

After conducting a partial intermediate cooling simulation, the result variables at the elements and the temperatures at the nodes of the blank are converted from volume elements to shell elements using Envyo[®] software (2.07.22). This conversion enhances the efficiency of the calculations for the forming and quenching phases. During the forming and quenching phase, process parameters such as holding time and pressing force are derived from experimental investigations, with a consistent Coulomb's friction value (μ) of 0.45 assumed. Another crucial aspect during the quenching phase is the heat transfer coefficient, which is integrated into the simulation as a function of the applied surface pressure, based on research conducted by Svec et al. [25].

4. Results

Mechanical properties, encompassing Vickers hardness, tensile strength, and elongation at break, are examined and analyzed in this section. The aim is to quantitatively assess the disparities in these mechanical properties exhibited by 22MnB5 blanks subjected to varying intermediate cooling durations (t_i). In addition to the examination of the mechanical properties, this section provides an assessment of temperature profiles and investigates

the microscopic structural images. Simultaneously, the results of the temperature profile and the hardness will serve the purpose of validating the numerical model.

4.1. Examination of the Temperature Profile and the Microstructure

The temperature profile of the blank serves as a crucial measured parameter for evaluating the phase transformation that takes place during cooling and for verifying the simulation. To measure the temperature of the blank, type K thermocouples from Herth GmbH Werne, Germany are affixed to the surface of the blank in both the heated and cooled areas. As depicted by the measurements in Figure 7, an increase in the partial intermediate duration (t_i) influences the temperature profile of the workpiece in both the heated and cooled regions.

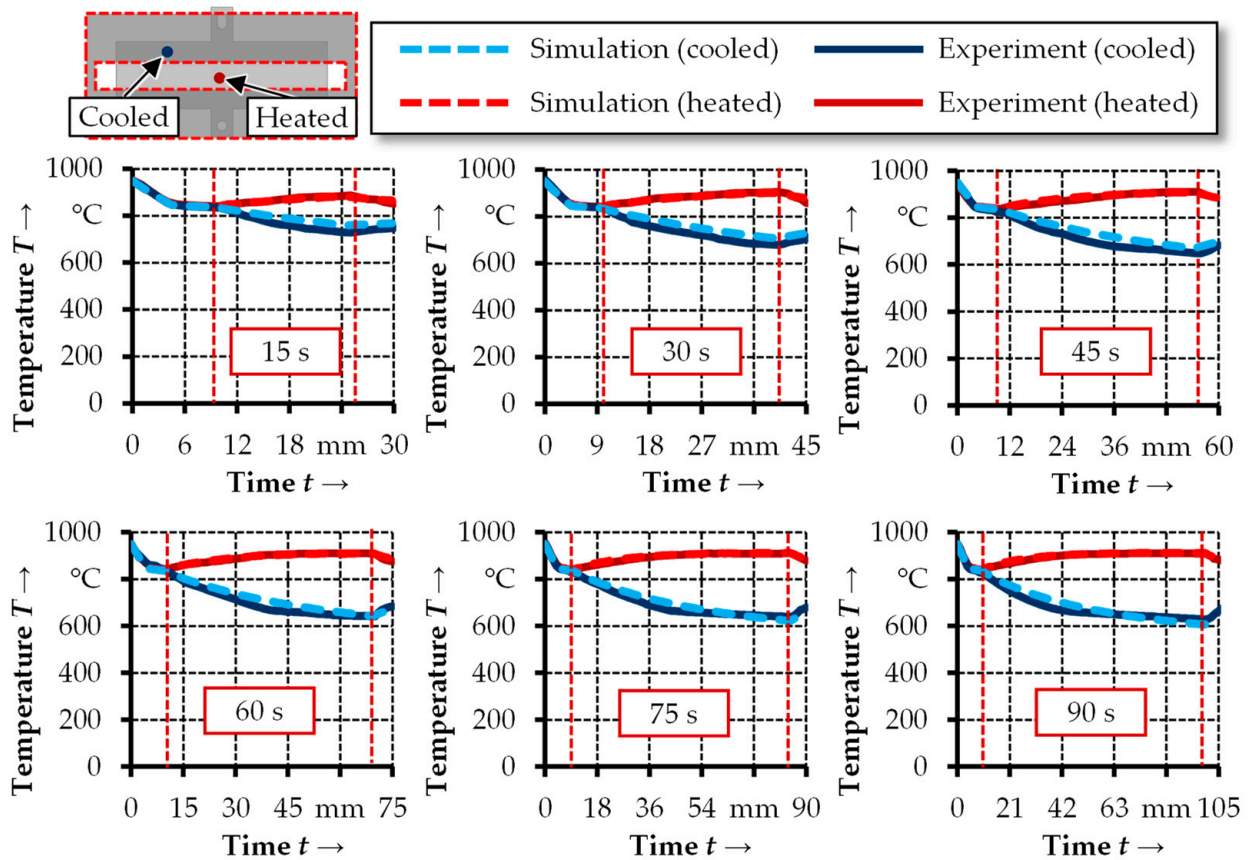


Figure 7. Experimentally determined and simulation-calculated time–temperature profiles at various partial intermediate cooling durations.

A comparison of the temperature profiles of the blanks at partial intermediate durations of 15 s, 30 s, and 45 s reveals a continuous temperature variation in both the heated and cooled regions. Increasing the partial intermediate cooling duration (t_i) from 15 s to 45 s, results in an increase in the blank temperature from 850 °C to 906 °C in the heated area and a decrease from 742 °C to 633 °C in the cooled area. Following a partial intermediate cooling duration (t_i) of 45 s, only minor temperature changes are observable at the measurement points due to the reduced cooling rate. The decreasing cooling rate over time in the covered area of the blank can be attributed to the declining emissivity coefficient over time, the increased temperature of the aluminum masks due to the absorption of thermal radiation, and the heat energy released during the phase transformation.

The numerical temperature profiles closely replicate the experimentally determined profiles in the heated and cooled areas with reasonable accuracy. The minor discrepancies between the simulation and experimental results can be attributed to the absence of the

temperature-dependent variation in the emission coefficient of the sheet surface in the simulation. Particularly with larger sheet thicknesses and longer partial intermediate cooling durations, assuming a constant emissivity coefficient can lead to an inaccurate calculation of the cooling rate in the covered area. Furthermore, the released latent heat due to the transformation of austenite into ferrite, pearlite, and bainite is not considered in the material model employed.

In addition to the temperature profiles of the blanks, Figure 8 provides corresponding microstructure images of the covered area at 10 mm from the edge of the hat profile. Nital etching is employed for this purpose in the study. The light microscopic images demonstrate that the partial intermediate cooling duration (t_i) significantly influences the phase transformation processes within the TemperBox[®]. Specifically, the sample with a partial intermediate duration (t_i) of 15 s exhibits a predominantly martensitic and bainitic structure, whereas an increasing proportion of ferrite and pearlite becomes evident in the overall structure starting from a partial intermediate duration (t_i) of 30 s. After a partial intermediate cooling duration (t_i) of 75 s, the presence of martensite and bainite phases can no longer be detected, resulting in the formation of a homogeneous structure comprising ferrite and pearlite phases.

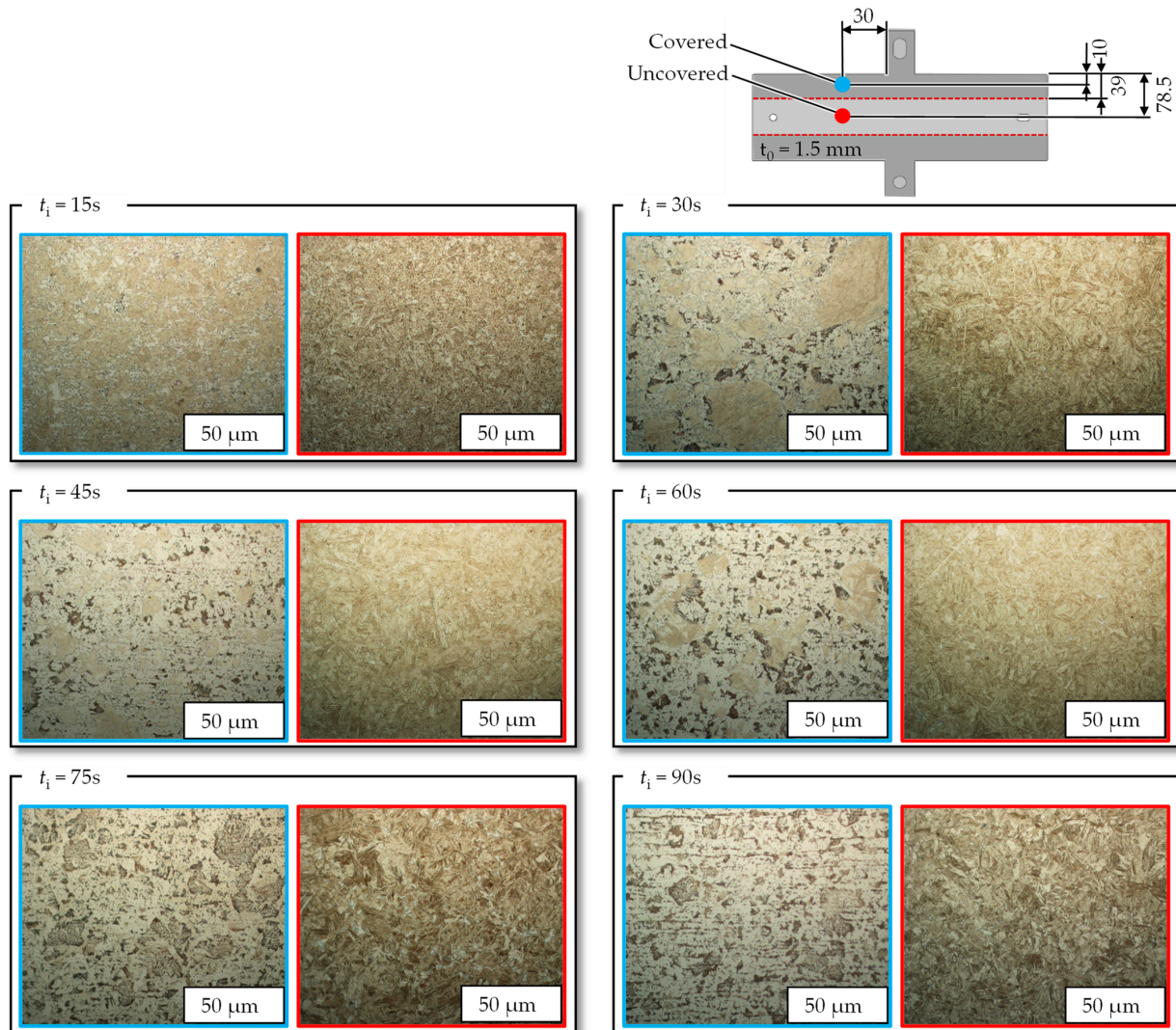


Figure 8. Microstructural images in the cooled region at varying intermediate cooling durations.

4.2. Analysis of the Mechanical Properties

An essential mechanical parameter for evaluating hot-stamped components is hardness, which enables the assessment of both the component's properties and the ensuing phase transformation. In this study, Vickers hardness tests were performed on cross-sections using the semi-automatic hardness tester DuraScan 70 G5 from Struers GmbH, in conjunction with the associated Ecos Workflow pro software from EMCO-TEST Prüfmaschinen GmbH Kuchl, Austria. The findings of the hardness measurements for different partial intermediate cooling durations are illustrated in Figure 9. Upon examining the results, it becomes evident that the hardness values in the uncovered area exhibit a consistent level of homogeneity, ranging from 415 HV to 522 HV for intermediate cooling durations of 15 s and 30 s. With an increasing partial intermediate cooling duration (t_i), the hardness values in the region between the covered and uncovered areas decrease by up to 35%, reaching values between 272 and 339 HV. In the covered area of the component, there is a noticeable decline in hardness, which is contingent upon the chosen partial intermediate cooling duration (t_i). The hardness values decrease gradually from the uncovered area to the covered area due to the directional internal heat conduction of the blank and radiative heat exchange between the cooled mask and the blank. From a partial intermediate cooling duration (t_i) of 45 s, no further reduction in hardness is observed in the covered area. Hardness values are reduced to as low as 185 HV. A partial intermediate cooling duration (t_i) of more than 45 s leads to more uniform hardness values in the covered area, resulting in a more distinct soft area in the component. This observation is consistent with the temperature profiles and microstructural images, which reveal no significant deviations from a partial intermediate cooling duration (t_i) of 45 s. To assess the differences between experiment and simulation, the numerically calculated hardness curves are compared with the experimentally determined hardness curves in Figure 9. The graphs show that the hardness curves can be calculated with a high degree of agreement. Similar to the experimental results, no decrease in hardness can be detected in the covered area from a partial intermediate cooling duration (t_i) of 45 s and beyond. Simultaneously, the numerical hardness curve also exhibits a distinct soft area from a duration of 45 s.

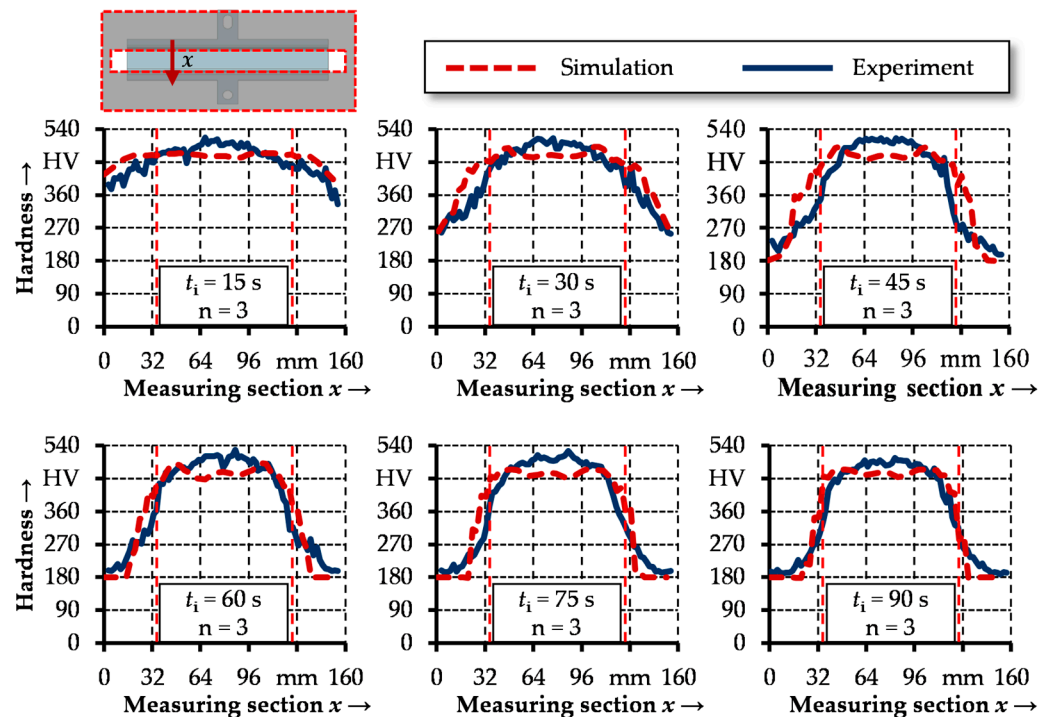


Figure 9. Simulatively calculated and experimentally determined hardness profiles.

A significant characteristic of tailored hot-stamped components is the transition zone between hard and soft areas, which can have a profound impact on component performance. Increasing the duration of partial intermediate cooling results in the formation of distinct hard and soft regions, characterized by narrower transition zones. This effect can be quantitatively determined through numerical calculations of the view factors and thermal interactions between the heating elements, masks, and the blank within the furnace chamber.

In addition to the hardness tests, tensile tests were conducted using a Z250 universal testing machine from Zwick/Roell AG. The resultant mechanical properties, namely tensile strength and elongation at break, are presented in Figure 10 for varying partial intermediate durations (t_i) in both the cooled and heated areas. Analysis of the graph reveals that in the covered area, the tensile strength decreases as the intermediate cooling duration (t_i) increases, up to 60 s. Concurrently, the elongation at break shows a significant increase starting from a duration of 60 s. Results obtained with cooling durations of 30 s and 45 s exhibit premature strain localization due to the strength's non-uniformity. The intermediate cooling durations of 30 s and 45 s do not allow the formation of a uniformly softened area across the width of the tensile specimen. This effect is confirmed by the higher standard deviation of the respective mean tensile strengths and elongations at break for the 30 s and 45 s intermediate cooling durations (t_i). The high standard deviation is due to the heterogeneous microstructure of martensite, bainite, ferrite, and pearlite. In the heated area, no discernible effect of the partial intermediate cooling on tensile strength and elongation at break is observed. This observation suggests the formation of a uniform martensitic microstructure in the uncovered area of the component, regardless of variations in the parameters.

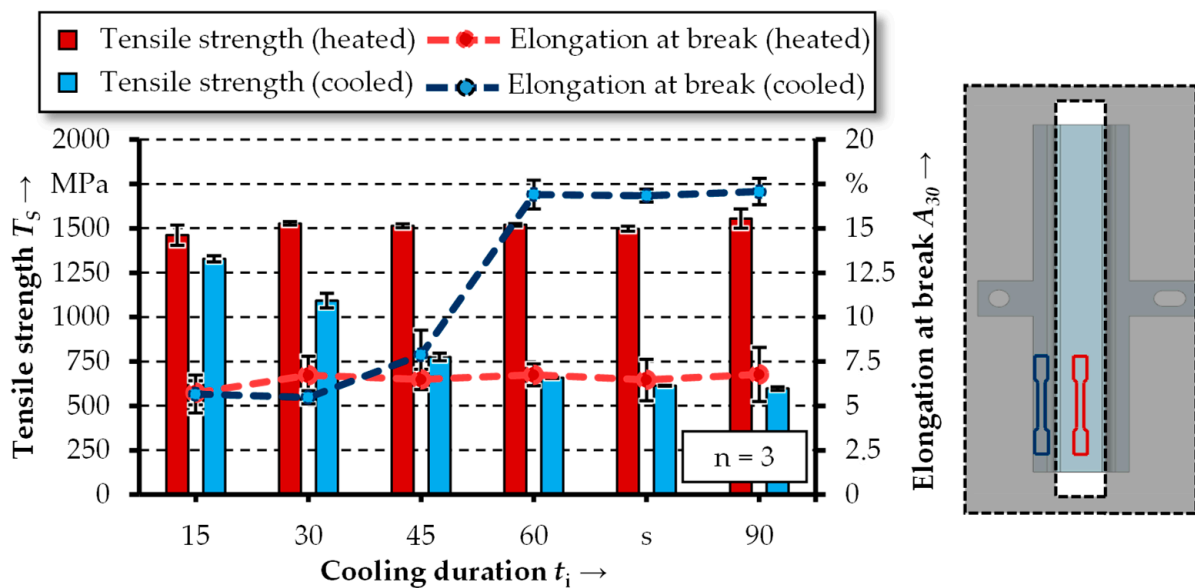


Figure 10. Tensile strength and elongation at break in the cooled and heated areas of the component.

During the forming phase, sheet thinning may occur due to the 7° wall angle. To measure the sheet thickness, cross-sections are taken under an optical microscope and then measured. To assess sheet thinning, the true thickness strain $\epsilon_t = \ln \frac{t_0}{t_1}$ is measured relative to the sheet thickness of 1.5 mm and plotted across the width of the component (Figure 11).

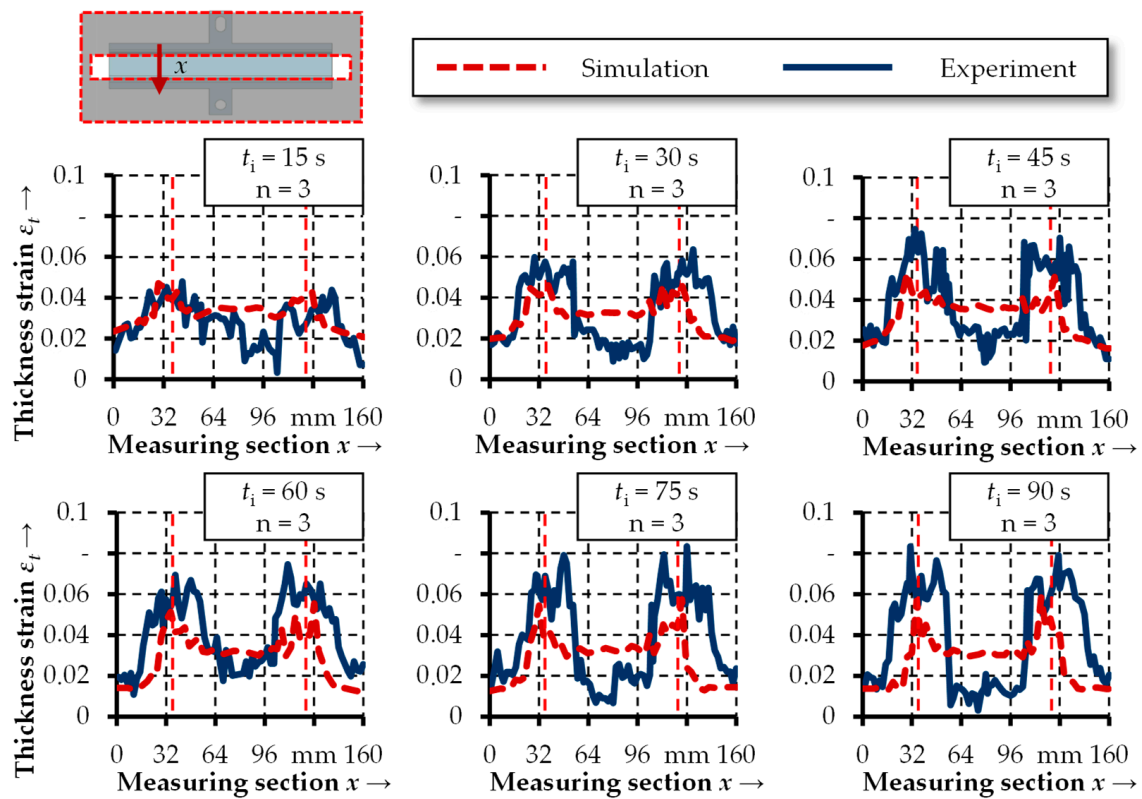


Figure 11. Thickness strain at the various intermediate cooling durations.

When examining the thickness strain profiles, a notable surge in strain becomes apparent within the wall regions at 20–40 mm and 120–140 mm. The increased sheet-thinning effect observed in the wall region is primarily due to constrained material flow resulting from intermediate cooling in the covered area of the component. This phenomenon induces the development of tensile stresses within the wall, resulting in increased sheet thinning and increased true strain values. To illustrate this further, Figure 12 shows the distribution of von Mises effective stresses (Figure 12a) and effective plastic strains (Figure 12b) for intermediate cooling durations (t_i) of 15 s and 45 s. For longer intermediate cooling durations (t_i), stresses locally increase in the wall region, causing uneven material flow in this region and ultimately leading to increased sheet thinning. Simultaneously, the distribution of effective plastic strain for 15 s and 45 s (Figure 12b) confirms an increase within the wall region with longer intermediate cooling durations (t_i).

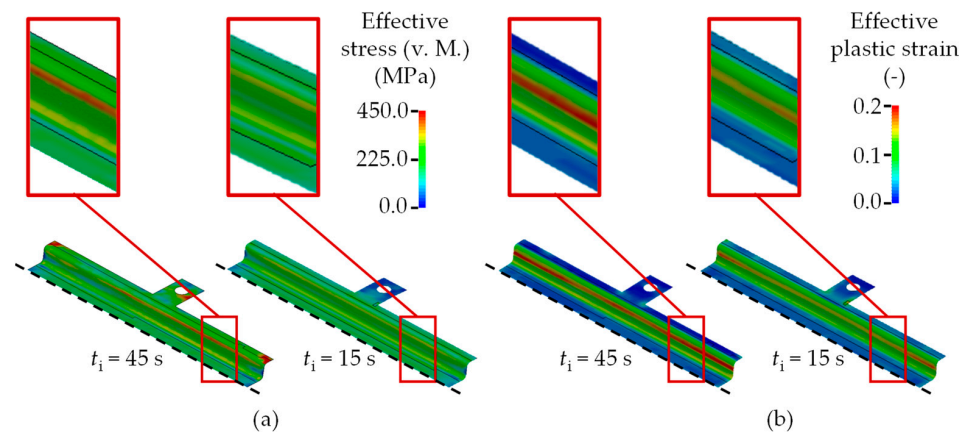


Figure 12. Distribution of the (a) effective stress and (b) effective strain after forming and quenching of the components.

Consequently, the increased implementation of partial intermediate cooling leads to an augmentation of the heterogeneity in strain and stress distribution within the wall region of the formed test component. To visualize the heterogeneity of the effective plastic strain, Figure 13 depicts the maximum effective plastic strain of the test component after quenching as a function of partial intermediate cooling. The analysis of the diagram (Figure 13) reveals that the maximum plastic strain increases to a value of 0.26 up to an intermediate cooling time of 45 s. Further increments in the intermediate cooling duration (t_i) do not yield a significant impact on the maximum plastic strain.

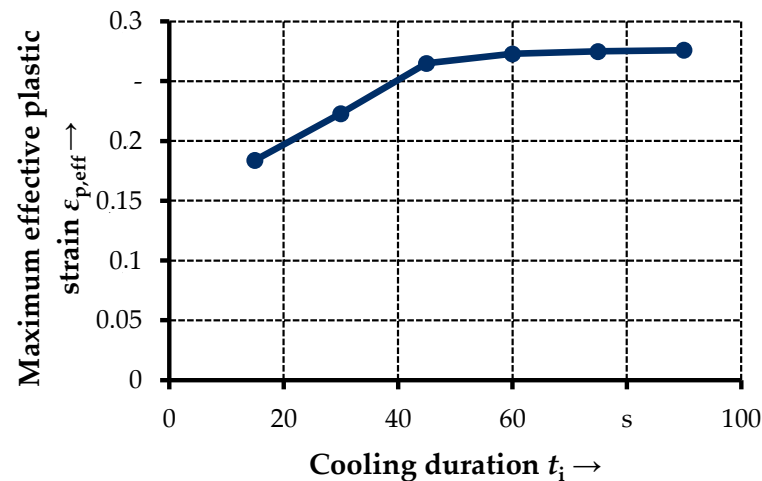


Figure 13. Maximum effective plastic strain as a function of cooling duration.

These findings suggest that local strain and consequent sheet thinning within the wall region can be addressed by numerical modeling. However, the numerical simulation consistently underestimates the thickness strain in comparison to the experimental outcomes across all parameter variations. In addition to the strain hardening behavior of the different phases, as derived from the research by Eller et al. [26] and integrated into the material model “*MAT_244”, the assumption of a constant Coulomb friction coefficient (μ) of 0.45 can have a pronounced effect on the numerical calculation of true strain profiles.

5. Conclusions

In summary, the present work has shown that the partial intermediate cooling duration in the TemperBox[®] has an influence on the phase transformation and the resulting mechanical properties. The results showed that the hardness values remained consistent in the uncovered area, but in the covered area of the hat profile, they decreased depending on the duration of partial intermediate cooling (t_i). Beyond 45 s of intermediate cooling, no further reduction in hardness was observed, leading to a more uniform hardness distribution in the covered area. These findings are in good agreement with both experimental and numerical data, demonstrating a distinct soft area in the component after 45 s of partial intermediate cooling. Additionally, this study demonstrated that partial intermediate cooling exerts an influence on the transition zone between hard and soft areas of the components, resulting in more distinct hard and soft areas and narrower transition areas with extended intermediate cooling durations. Furthermore, an approach to simulate the partial intermediate cooling with the TemperBox[®] was presented and validated. Overall, the combination of the view factor calculation and the use of the material model “*MAT_244” is suitable for the prediction of the semi-finished product temperature and the Vickers hardness after tailored tempering with intermediate cooling. The tensile tests confirmed the results from the measured hardening profiles and showed that the tensile strength in the covered area decreased with increasing intermediate cooling duration up to 60 s, while the elongation at break increased significantly from 60 s onwards. It is also evident that the duration of intercooling impacts the true strain in the thickness direction within the wall region of

the component. A longer intermediate cooling duration of up to 45 s results in a higher thickness stress, mainly due to the increased heterogeneity of stress and strain in the wall region of the test component. In the simulation, the thickness strain is underestimated. For components with more complex boundary conditions in terms of geometry and tool contact, it is necessary to apply a strain rate, temperature- and phase-dependent hardening behavior, and a pressure- and temperature-dependent coefficient of friction.

Author Contributions: Conceptualization, A.R.; methodology, A.R.; software, A.R.; validation, A.R.; formal analysis, A.R.; investigation, A.R.; resources, A.R.; data curation, A.R.; writing—original draft preparation, A.R.; writing—review and editing, A.R., S.H., T.S. and M.M.; visualization, A.R.; supervision, S.H., T.S. and M.M.; project administration, A.R., S.H., T.S. and M.M. All authors have read and agreed to the published version of the manuscript.

Funding: This research received no external funding.

Data Availability Statement: All data supporting the reported results are available in the paper.

Conflicts of Interest: Authors Alborz Reihani, Sebastian Heibel, and Thomas Schweiker are employees of the company Mercedes-Benz (Germany). The remaining author declares that the research was conducted in the absence of any commercial or financial relationships that could be construed as a potential conflict of interest.

References

- Haddadian, G.; Khodayar, M.; Shahidehpour, M. Accelerating the Global Adoption of Electric Vehicles: Barriers and Drivers. *Electr. J.* **2015**, *28*, 53–68. [CrossRef]
- United Nations General Assembly. Resolution A/RES/74/299 Improving Global Road Safety. 2020. Available online: <https://frsc.gov.ng/wp-content/uploads/2021/02/UNGA-Resolution-2020.pdf> (accessed on 19 October 2023).
- Taylor, T.; Clough, A. Critical review of automotive hot-stamped sheet steel from an industrial perspective. *Mater. Sci. Technol.* **2018**, *34*, 809–861. [CrossRef]
- Karbasian, H.; Tekkaya, A.E. A review on hot stamping. *J. Mater. Process. Technol.* **2010**, *210*, 2103–2118. [CrossRef]
- Omer, K.; Kortenaar, L.; Butcher, C.; Worswick, M.; Malcolm, S.; Detwiler, D. Testing of a hot stamped axial crush member with tailored properties Experiments and models. *Int. J. Impact Eng.* **2017**, *103*, 12–28. [CrossRef]
- Merklein, M.; Wieland, M.; Lechner, M.; Bruschi, S.; Ghiotti, A. Hot stamping of boron steel sheets with tailored properties: A review. *J. Mater. Process. Technol.* **2016**, *228*, 11–24. [CrossRef]
- Nakagawa, Y.; Mori, K.; Suzuki, Y.; Shimizu, Y. Tailored tempering without die heating in hot stamping of ultra-high strength steel parts. *Mater. Des.* **2020**, *192*, 108704. [CrossRef]
- Wu, S.; Bardelcik, A.; Chiriac, C.; Elsayed, A.; Shi, C. The effect of heating rate and coating weight on the intermetallic growth of Al-Si coated hot stamping steel. *Surf. Coat. Technol.* **2023**, *471*, 129913. [CrossRef]
- Hu, P.; Ma, N.; Liu, L.Z.; Zhu, Y.G. Hot Forming Simulation Algorithms of High-Strength Steels. In *Theories, Methods and Numerical Technology of Sheet Metal Cold and Hot Forming*; Hu, P., Ma, N., Liu, L.Z., Zhu, Y.G., Eds.; Springer: London, UK, 2013; pp. 113–151. [CrossRef]
- Hagenah, H.; Merklein, M.; Lechner, M.; Schaub, A.; Lutz, S. Determination of the mechanical properties of hot stamped parts from numerical simulations. *Procedia CIRP* **2015**, *33*, 167–172. [CrossRef]
- Hart-Rawung, T.; Buhl, J.; Horn, A.; Bambach, M.; Merklein, M. A unified model for isothermal and non-isothermal phase transformation in hot stamping of 22MnB5 steel. *J. Mater. Process. Technol.* **2023**, *313*, 117856. [CrossRef]
- Liu, G.; Zhang, D.; Yao, C. A modified constitutive model coupled with microstructure evolution incremental model for machining of titanium alloy Ti-6Al-4V. *J. Mater. Process. Technol.* **2021**, *297*, 117262. [CrossRef]
- Fanfoni, M.; Tomellini, M. The Johnson-Mehl-Avrami-Kohnogorov model: A brief review. *Nouv. Cim. D* **1998**, *20*, 1171–1182. [CrossRef]
- Bok, H.H.; Kim, S.N.; Suh, D.W.; Barlat, F.; Lee, M.G. Non-isothermal kinetics model to predict accurate phase transformation and hardness of 22MnB5 boron steel. *Mater. Sci. Eng.* **2015**, *626*, 67–73. [CrossRef]
- Li, M.V.; Niebuhr, D.V.; Meekisho, L.L.; Atteridge, D.G. A computational model for the prediction of steel hardenability. *Metall. Mater. Trans. B* **1998**, *29*, 661–672. [CrossRef]
- Kirkaldy, J.S.; Venugopalan, D. Prediction of microstructure and hardenability in low alloy steels. In *International Conference on Phase Transformations in Ferrous Alloys*; Marder, A.R., Goldstein, J.I., Eds.; Metallurgical Society of AIME: Philadelphia, PA, USA, 1983; pp. 125–148.
- Koistinen, D.P.; Marburger, R.E. A general equation prescribing the extent of the austenite-martensite transformation in pure iron-carbon alloys and plain carbon steels. *Acta Metallurgica* **1959**, *7*, 59–60. [CrossRef]
- Baehr, H.D.; Stephan, K. *Heat and Mass Transfer*; Springer: Berlin/Heidelberg, Germany, 2006; pp. 545–658. [CrossRef]

19. Glass, M.W. *CHAPARRAL: A Library for Solving Large Enclosure Radiation Heat Transfer Problems*; Sandia National Laboratories: Albuquerque, NM, USA, 1995. [[CrossRef](#)]
20. Maynier, P.; Jungmann, B.; Dollet, J. Creusot-Loire system for the prediction of the mechanical properties of low alloy steel products. In *Hardenability Concepts with Applications to Steel*; Doane, D.V., Kirkaldy, J.S., Eds.; Metallurgical Society of AIME: Warrendale, PA, USA, 1978; pp. 518–545.
21. Åkerstrom, P.; Oldenburg, M. Austenite decomposition during press hardening of a boron steel—Computer simulation and test. *J. Mater. Process. Technol.* **2006**, *174*, 399–406. [[CrossRef](#)]
22. Aranda, L.G.; Chastel, Y.; Pascual, J.F.; Negro, T.D. Experiments and Simulation of Hot Stamping of Quenchable Steels. In *Proceedings of the 7th International Conference on Technology of Plasticity, Yokohama, Japan, 27 October–1 November 2002*; pp. 1135–1140.
23. Blankenhorn, G.; Gyesi, B.; Malcolm, S.; Gandikota, I.; Grimes, R.; Rouet, F.H. Validation of a Thermal Radiation Problem using *BOUNDARY_RADIATION_ENCLOSURE. In *Proceedings of the 12th European LS-DYNA Conference, Koblenz, Germany, 14–16 May 2019*.
24. Kabelac, S.; Vortmeyer, D. *VDI Heat Atlas*, 2nd ed.; Springer: Berlin/Heidelberg, Germany, 2010; pp. 945–960. [[CrossRef](#)]
25. Merklein, M.; Svec, T. Hot stamping: Manufacturing functional optimized components. *Prod. Eng. Res. Devel.* **2013**, *7*, 141–151. [[CrossRef](#)]
26. Eller, T.K.; Greve, L.; Anders, M.T.; Medricky, M.; Hatscher, A.; Meinders, T. Constitutive modeling of quench-hardenable boron steel with tailored properties. In *Proceedings of the 6th Forming Technology Forum, Herrsching, Germany, 19–20 September 2013*; pp. 1–6.

Disclaimer/Publisher’s Note: The statements, opinions and data contained in all publications are solely those of the individual author(s) and contributor(s) and not of MDPI and/or the editor(s). MDPI and/or the editor(s) disclaim responsibility for any injury to people or property resulting from any ideas, methods, instructions or products referred to in the content.